Supporting Information

Boosting Electrochemical Methane Conversion by Oxygen Evolution Reactions on Fe-N-C Single Atom Catalysts

Cheolho Kim[1,†], Heewon Min[1,†], Junmin Kim[1,†] and Jun Hyuk Moon[1*]

[1]Department of Chemical and Biomolecular Engineering, Institute of Emergent Materials, Sogang University, Baekbeom-ro 35, Mapo-gu, Seoul, 04107, Republic of Korea.

Corresponding Author

*Corresponding author, E-mail: junhyuk@sogang.ac.kr

[†]These authors equally contributed to this work

Supplementary note #1

Preparation of Fe-N-C SAC. ZIF-8 was obtained by reaction of 2-methylimidazole (16 mmol, Sigma-Aldrich) and Zinc nitrate hexahydrate (4 mmol, $Zn(NO_3)_2$ $6H_2O$, Sigma-Aldrich) in 45 ml methanol.[1] The addition of iron(III) acetylacetonate ($Fe(acac)_3$, 0.4 mmol, Sigma-Aldrich) to this solution contained $Fe(acac)_3$ in the molecular cage of ZIF-8 during the self-assembled formation of ZIF-8. The diameter of the cage is 11.6 Å, which is comparable to the size of $Fe(acac)_3$ about 10 Å. As a result, one $Fe(acac)_3$ molecule is included in the cage. The reaction lasts about 3 hr with vigorous stirring. The precipitate, $Fe(acac)_3$-impregnated ZIF-8, is dried in a 50 °C oven. The dried sample was annealed at 900°C in an Ar atmosphere. During this process, ZIF-8 was converted to nitrogen-doped carbon, and $Fe(acac)_3$ is thermally reduced to Fe, where Fe binds to the nitrogen site to form a Fe-N-C SAC.

Analysis of electrochemical methane conversion. The linear sweep voltammetry (LSV) was recorded using a potentiostat (Versastat Ametek): the scan rate was 0.02 V/s. The LSV was achieved using a three-electrode system; A Fe-N-C catalyst-coated carbon substrate (1x1 cm^2) was used as a working electrode, Pt as a counter electrode, and a reversible hydrogen electrode (RHE) as a reference electrode. An electrolyte of 0.1M KOH was utilized. The saturation of methane in the electrolyte was achieved by aeration of methane using a microsparger; The aeration was carried out at 25 °C for 30 min. The electrochemical impedance spectrum (EIS) was recorded with an impedance analyzer (Versastat, Ametek); the frequency was scanned in the range 1MHz - 0.1Hz, and the voltage amplitude was set to 10mV. The electrochemical methane conversion was performed by immersing the Fe-N-C catalyst electrode, Pt counter electrode, and RHE reference electrode in a gas-tight reactor containing a methane-saturated electrolyte; The reaction temperature is 25 °C.

Analysis of the product. Gas Chromatography-Mass spectra were recorded using Gas Chromatography (GC-MS, 7890B-5977A, Agilent Technologies, USA) equipped with a mass selective detector MSD 5975 (electron impact ionization, EI, 70 eV, Agilent Technologies). A fused-silica capillary (DB-WAX, 0.25 μm thick poly(ethyleneglycol) coating, Agilent Technologies, USA) was exploited. Samples were injected by headspace sampling (1000 ul of a sample heated at 70 °C for 30 minutes); The injection temperature is 250 °C. The carrier gas is helium (1 mL/min, 99.999%), and the dilution ratio is 8:1 (sample: He). The oven temperature conditions are 5 min at 40 °C, 4 °C/min (100 °C), and 3 min at 240 °C (20 °C/min).

The production rate is calculated using the concentration of the products in the electrolyte measured by GC/MS, and the specific equation is as follows:

$$\text{Production rate } (\mu\text{mol} \cdot g_{cat}{}^{-1} \cdot h^{-1}) = \frac{C_{product} \times V \times \rho_{product}}{M_{product} \times m_{Fe}} \times 10^6$$

where $C_{product}$ (ppm) is the concentration of the product ethanol, V (mL) is the volume of electrolyte, $\rho_{product}$ (g·mL^{-1}) is the density of ethanol, $M_{product}$ (g·mol^{-1}) is the molar mass of ethanol and m_{Fe} is the Fe single atom mass of working electrode.

Analysis using isotopes. The reaction was carried out using $^{13}CH_4$ (Sigma-Aldrich, 99 %, 99 atom% ^{13}C), where a D_2O-based electrolyte is employed. The liquid product containing isotopes was recorded with NMR (Avance III HD 400 FT-NMR instrument, Bruker Biospin). The proton high power decoupling field strength was 11.7 (5.0 μs length 90° 1H pulse); The contact time was 4 ms at the Hartmann-Hahn matching condition 50 kHz, and the scan delay time was 3 s; The 13C chemical shift was analyzed for accuracy of ± 0.5 ppm; Tetramethylsilane (TMS) was applied as standard; The calibration was performed with the residual signal of 3-(trimethylsilyl)-1-propane sulfonic acid sodium salt (DSS) at δ = 0.0 ppm.

Characterization. The scanning electron microscope (SEM) was recorded using a JSM-7800F (JEOL). The transmission electron microscope (TEM) was recorded using a JEM-ARM200F (JEOL); The microscope was equipped with a spherical aberration corrector in the condenser lens (probe corrector). The high-angle annular dark field-scanning TEM (HAADF-STEM) was conducted by using a JEM-ARM200F (JEOL) microscope at an acceleration voltage of 200 kV. The EDS mapping was recorded using Oxford Instruments X-Max SDD. The XRD was recorded using a Rigaku miniflex-2005G303 X-ray diffractometer (Cu Kα radiation at 20 kV and 10 mA) in the 2 theta range of 25-65°. The XPS was analyzed by using a Leybold photoelectron spectroscopy (Al Ka monochromatic beam). The X-ray absorption fine structure(XAFS) measurements were performed to probe the valence state and the coordination of iron species at the 7D XAFS beamline of the Pohang Light Source (PLS-II) in the 3.0 GeV storage ring. The XAFS spectra were collected in fluorescence mode. The obtained spectra were processed using Demeter software. Extended x-ray absorption fine structure (EXAFS) spectra were fitted using Artemis software in the k-space range of 3-14 Å. Gas Chromatography-Mass spectra were recorded using Gas Chromatography(GC-MS, 7890B-5977A, Agilent Technologies, USA) equipped with a mass selective detector MSD 5975(electron impact ionization, EI, 70Ev, Agilent Technologies). A fused-silica capillary (DB-WAX, 0.5 μm thick poly(ethyleneglycol) coating, Agilent Technologies, USA) was exploited. The sample injection temperature was set at 250 °C. The carrier gas is helium(1 mL/min, 99.999%), and the dilution ratio is 10:1 (sample: He). The oven temperature conditions are 5 min at 40 °C, 4 °C/min (100 °C), and 3 min at 240 °C (20 °C/min).

DFT calculation. All calculations were performed using the Quantum ESPRESSO package based on density functional theory. The projector augmented (PAW) method[2], and the Generalized gradient approximation (GGA) with the Perde-Burke-Ernzerhof (PBE) exchange-correlation functional was used.[3] Plane-wave basis set with a cutoff energy of 30 Ry was employed. The k-point set of (2 ×2 ×1) selected by the Monkhorst-Pack scheme was used to obtain Brillouin zone integration. For structure optimization, all ions were relaxed until a maximum force of 0.005 eV/Å. Specifically, a SAC was applied embedding the Fe-N4 site into periodic 6×6 graphene support with lattice parameters a=b=12.78 Å The vacuum spacing was set to be 15 Å along the z direction to avoid the interactions between neighboring slabs. The standard Gibbs free energy change was obtained using the equation: $\Delta G = \Delta E + \Delta ZPE - T\Delta S$ where ΔE, ΔZPE, and ΔS were the reaction energy, the change in zero point energy, and the change in entropy, respectively.[4]

Microkinetic analysis

We analyze the surface coverage of OER intermediates according to anodic potential on Fe-N-C single atom catalyst by microkinetic analysis. Under the condition that the OOH* formation is the rate-determining step, we apply a steady-state approximation to the formation reactions of OH* and O*.

$$k_1\theta_* = k_{-1}\theta_{OH*}$$

$$k_2\theta_{OH*} = k_{-2}\theta_{O*}$$

Here, k_1 and k_{-1} are rate constants for OH* formation and its reverse reaction, respectively, k_2 and k_{-2} are rate constants for O* formation and its reverse reaction, respectively, Θ_{OH*} and Θ_{OH*} stand for coverage for OH* and O*, respectively.

We also define equilibrium constants (K_1 and K_2) for these reactions.

$$K_1 = \frac{\theta_{OH*}}{\theta_*}$$

$$K_2 = \frac{\theta_{O*}}{\theta_{OH*}}$$

Rearranging these equations using the statement of site conservation ($\sum_i \theta_i = 1$), we arrive at the equations for Θ_{OH*} and Θ_{OH*} expressed as equilibrium constants.

Combining the Gibbs energy equation in the reaction ($\Delta G_i = -RTlnK_i$) and also the change in the Gibbs energy with the potential at the electrode ($\Delta G_i(U) = \Delta G_i(0) \pm eU$), we get the equations for Θ_{OH*} and Θ_{OH*} as a function of the electrode potential.

Supplementary note #2

Mechanism for the ethanol-to-acetone conversion reaction.

$$CH_3CH_2OH^* \xrightarrow{-H^+} CH_3CHOH^* \xrightarrow{-H^+} CH_3COH^* \xrightarrow{-H^+} CH_3CO^* \quad (1)$$

$$CH_3CO^* + O^* + CH_4 \rightarrow CH_3CO^* + OH^* + {CH_3}^* \rightarrow CH_3COCH_3 + OH^* \quad (2)$$

(1) Ethanol is converted to CH_3CO^* by a continuous deprotonation reaction. (2) The CH_3CO^* reacts with activated methane to form acetone.

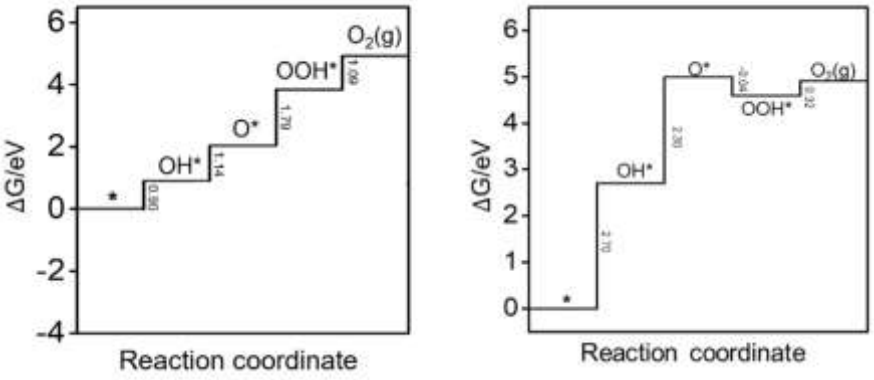

Figure S1. Comparison of energy profiles for OER on (left) Fe-N-C single atom catalysts and (right) Fe_2O_3 catalysts

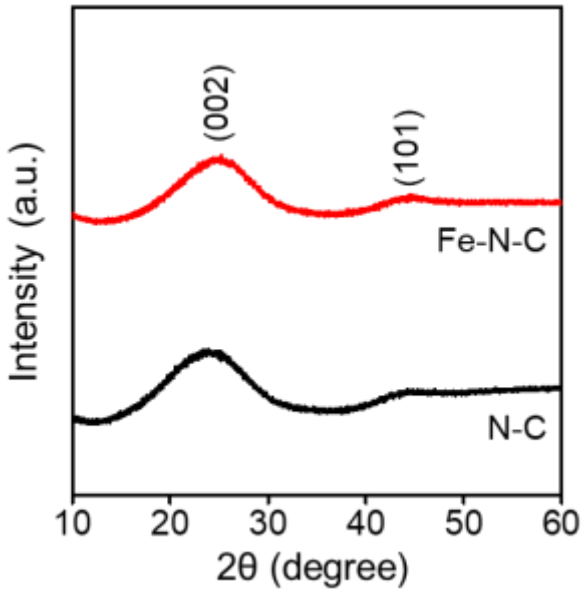

Figure S2. XRD spectra of Fe-N-C and N-C catalysts.

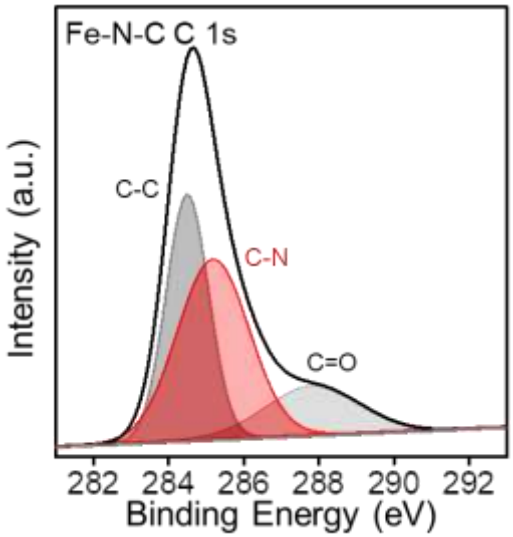

Figure S3. C 1s XPS spectrum of Fe-N-C catalysts. The spectrum is deconvolved into peaks for C=O, C-N, and C=O. In particular, the C–N peaks indicate nitrogen doping on graphitic carbon.

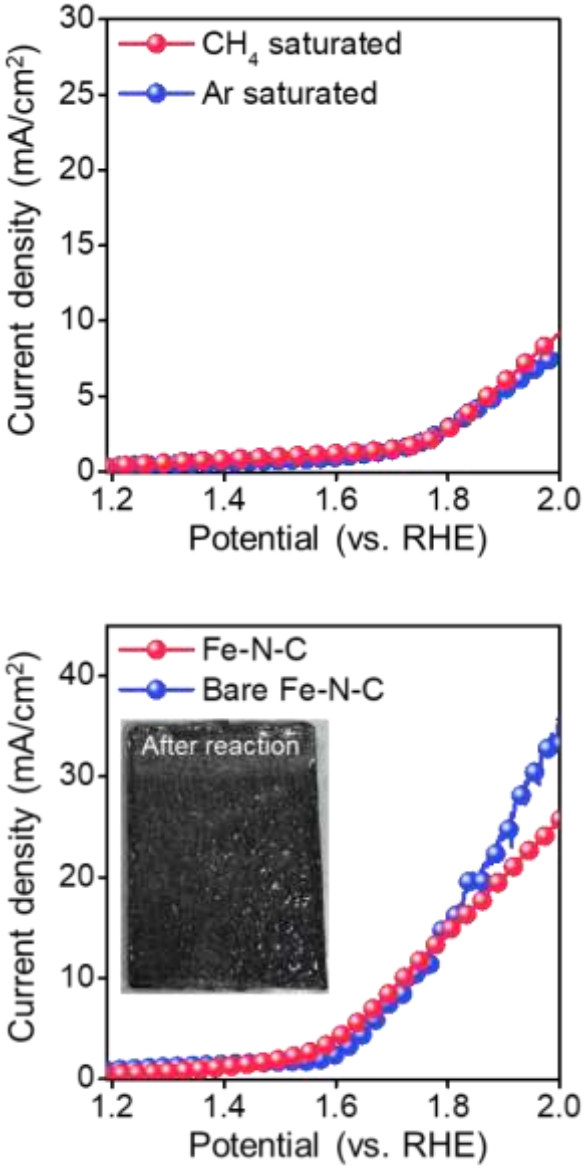

Figure S4. (Top) LSV profiles of Nafion-coated electrodes in methane and Ar-saturated electrolyte. (Bottom) LSV profile of Fe-N-C catalyst electrodes prepared without Nafion in methane-saturated electrolyte, with the LSV of Fe-N-C catalyst electrodes prepared with Nafion binder included for comparison. The bare Fe-N-C catalyst exhibits an unstable LSV profile. Inset image displays a digital camera image of the Fe-N-C catalyst electrode prepared without Nafion after the reaction, revealing the detachment of the catalyst from the graphite foil substrate.

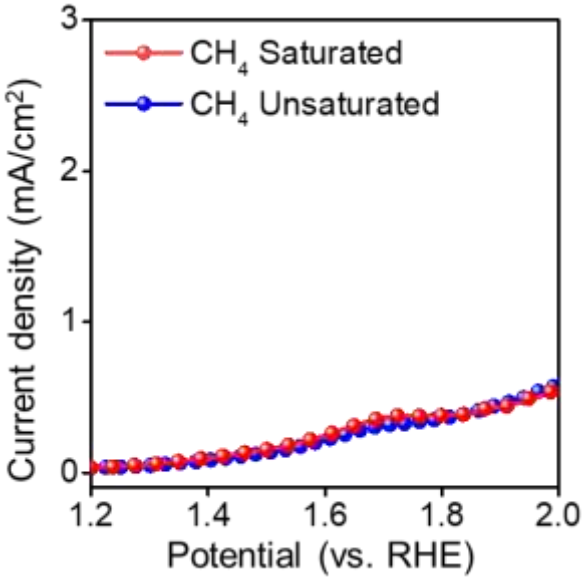

Figure S5. LSV curves of N-C with and without methane saturation in the electrolyte. Unlike the LSV for Fe-N-C catalysts, the LSV profile in methane-saturated electrolytes overlaps with that in methane-free electrolytes. As a result, the N-C catalyst shows no electrochemical activity.

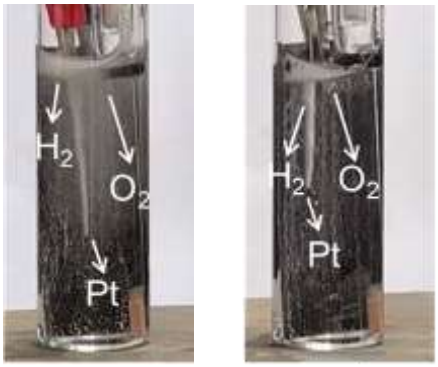

Figure S6. (left) Digital camera image of the electrodes at the application of 2.0 V_{RHE} potential in a bare electrolyte not saturated with methane; vigorous bubbling of H_2 and O_2 gases is observed at the Pt counter electrode and Fe-N-C catalyst electrode, respectively. (right) (left) Digital camera image of the electrodes at the application of 2.0 V_{RHE} potential in the methane-saturated electrolyte. The bubbling of O_2 is relatively weak, revealing the formation of a liquid product by methane oxidation.

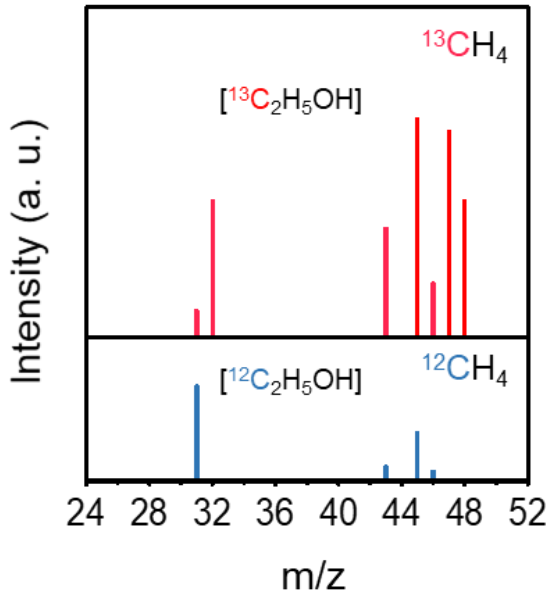

Figure S7. GC-MS spectrum of the ethanol product from the reaction with $^{13}CH_4$. The peaks shifted by m/z by one are identified, which correspond to ethanol containing ^{13}C.

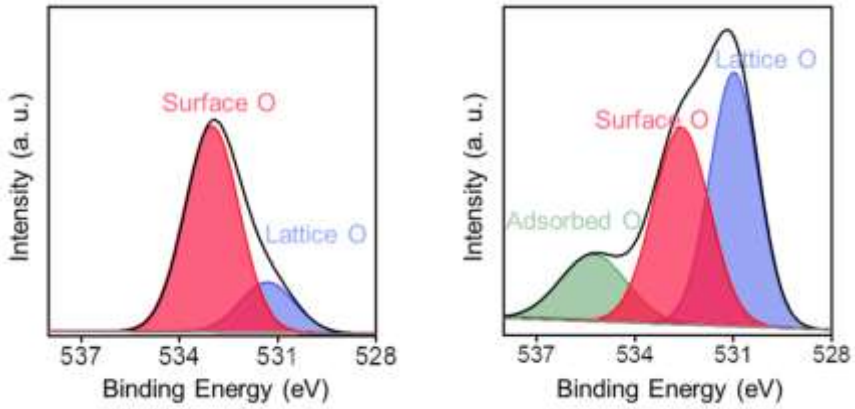

Figure S8. Ex-situ O 1s XPS spectra of Fe-N-C single atom catalysts (Left) with and (Right) without electrochemical potential applied. The Fe-N-C catalyst with applied potential clearly shows peaks for the adsorbed oxygen species, confirming the adsorption of O* by electrochemical OER.

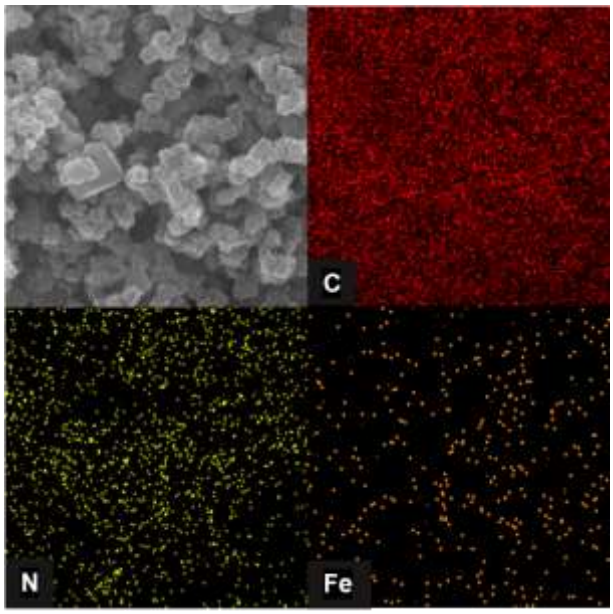

Figure S9. SEM / EDS mapping images of the Fe-N-C single atom catalysts coated on GDE.

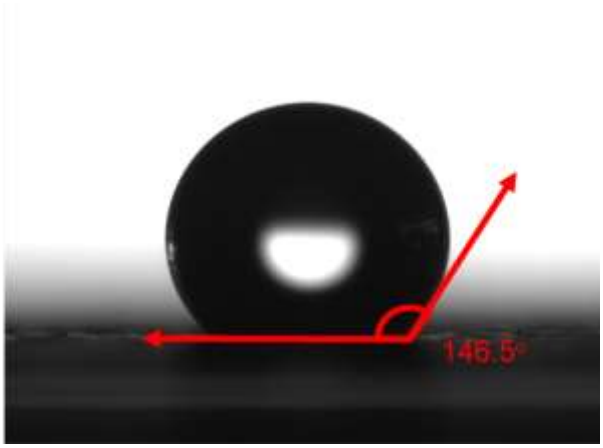

Figure S10. Contact angle photograph of Fe-N-C catalyst-coated GDE. The catalyst-coated GDE film exhibits very hydrophobicity with a contact angle of 147°.

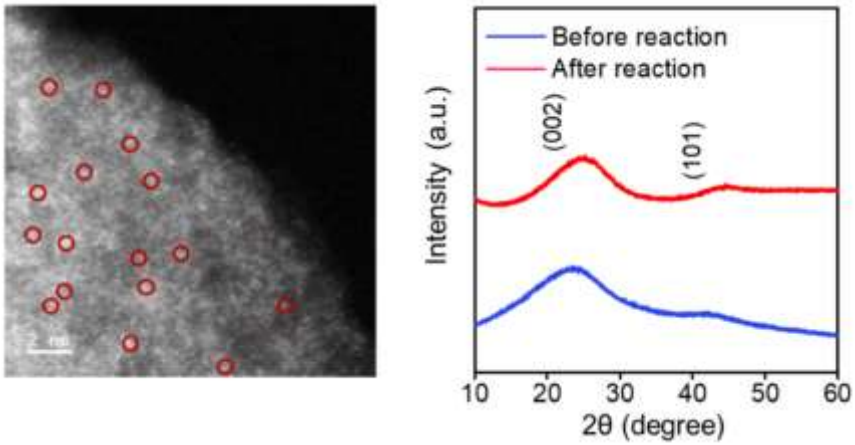

Figure S11. (a) HAADF-STEM image and XRD pattern of the Fe-N-C single atom catalyst after the long-term reaction.

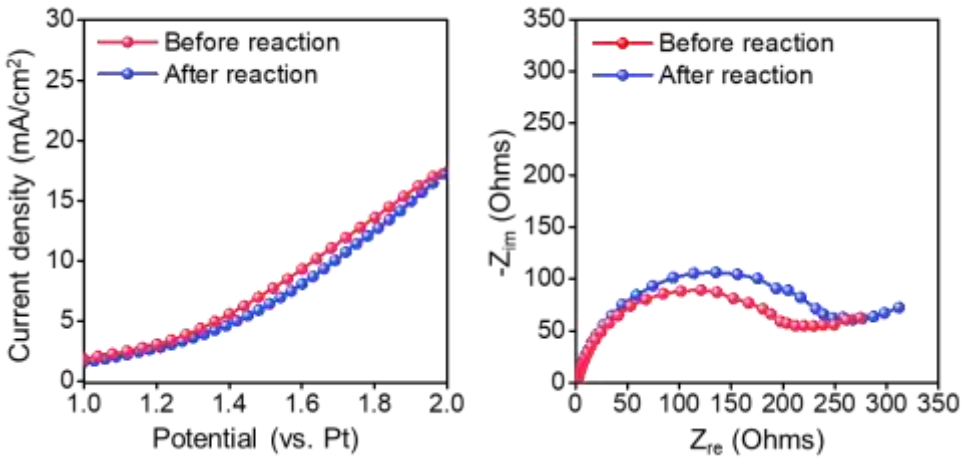

Figure S12. (Left) LSV and (Right) EIS profiles of the Fe-N-C single-atom catalyst electrode in the flow cell before and a 100-hour reaction. After the reaction, the LSV profile nearly overlaps with the pre-reaction profile, confirming the sustained electrochemical activity at the catalyst electrode during the reaction. In the EIS spectra, we compare the charge transfer resistance (Rct) values corresponding to the semicircle size; after the reaction, Rct increases by approximately 10%; this may be associated with changes in wettability towards the electrolyte in the gas diffusion electrode.

Table S1. Comparison of FE in OER-assisted electrochemical methane conversion

Catalysts	Electrolyte	Temperature	Pressure (atm)	Faradaic Efficiency (%)	Ref
Fe-N-C Single Atom	0.1M KOH	RT	1	46.1	Our work
Rh/ZnO	0.1M KOH	RT	1	10	[5]
Mg-MOF-74	1M KOH	RT	1	10.9	[6]
Cu_2O_3/TiO_2	0.1M KOH	RT	1	6	[7]

Table S2. Comparison of production rates in electrochemical methane-alcohol conversion for various catalysts.

Catalysts	**Methane activation**	**Ethanol production rate ($\mu mol \cdot g_{cat}^{-1} \cdot hr^{-1}$)**	**Ethanol selectivity (%)**	**Reaction condition**	**Ref.**
Fe-N-C Single atom	Electrocatalytic	4668.3 11480.6 (flow cell)	85 87% (flow cell)	25°C, 1bar	Our work
NiO/Ni	Electrocatalytic	25	77	25°C, 1bar	[8]
NiO/ZrO_2	Electrocatalytic	-	-	40°C, 1bar	[9]
ZrO_2-NT/Co_3O_4	Electrocatalytic	2416(propanol)	34(propanol) 10(methanol)	25°C, 1bar	[10]
$TiO_2/RuO_2/V_2O_5$	Electrocatalytic	297(methanol)	97	25°C, 1bar	[11]
Rh/ZnO	Electrocatalytic	789	85	25°C, 1bar	[5]
CuO/CeO_2	Electrocatalytic	1009.8(methanol)	83(methanol)	25°C, 1bar	[12]

Cu/Al_2O_3 @NH_4BF_4	Electrocatalytic	3095	85	25℃, 1bar	[13]
$Co_{0.6}Ni_{0.4}Fe_2O_4$-N/C	Electrocatalytic	1925.4 (methanol)	83 (methanol)	20℃, 1bar	[14]
IrO_2/CuO	Thermocatalytic	290.7(methanol)	95(methanol)	150℃, 3bar	[15]
Fe-MFI zeolite	Thermocatalytic	948.8(methaol)	85(methanol)	50℃, 30bar	[16]
Pd-Au nanoparticles	Thermocatalytic	278(methanol)	73.2(methanol)	150℃, 33bar	[17]
Fe-ZSM-5	Thermocatalytic	1520(methanol)	6.9(methanol)	50℃, 31bar	[18]
Hap	Thermocatalytic	84.4(methanol)	61.5(methanol)	25℃, 1bar	[19]
IrO_2/ZnO/CuO	Thermocatalytic	179(methanol)	59(methanol)	150℃, 3bar	[20]
Au/BP nanosheets	Photocatalytic	56.8(methanol)	99(methanol)	90℃, 33bar	[21]
FeOOH/ m-WO_3	Photocatalytic	238.6(methanol)	91(methanol)	25℃, 1bar	[22]
TiO_2	Photocatalytic	471(methanol)	83(methaol)	30℃, 30bar	[23]

Cu-PCN	Photocatalytic	106	81	25℃, 1bar	[24]
$BiOCl\text{-}O_v$	Photocatalytic	180.75 (methanol)	80 (methanol)	25℃, 1bar	[25]

References

1. Y. Chen, S. Ji, Y. Wang, J. Dong, W. Chen, Z. Li, R. Shen, L. Zheng, Z. Zhuang and D. Wang, *Angew. Chem.*, 2017, **129**, 7041-7045.
2. B. Hammer, L. B. Hansen and J. K. Nørskov, *Phys. Rev. B*, 1999, **59**, 7413-7421.
3. W. Luo, C. Jiang, Y. Li, S. A. Shevlin, X. Han, K. Qiu, Y. Cheng, Z. Guo, W. Huang and J. Tang, *J. Mater. Chem. A*, 2017, **5**, 2021-2028.
4. M. Li, L. Zhang, Q. Xu, J. Niu and Z. Xia, *J. Catal.*, 2014, **314**, 66-72.
5. Z. Xie, M. Chen, Y. Chen, A. Guan, Q. Han and G. Zheng, *J. Phys. Chem. C*, 2021, **125**, 13324-13330.
6. M. Chen, X. Lv, A. Guan, C. Peng, L. Qian and G. Zheng, *J. Colloid Interface Sci.*, 2022, **623**, 348-353.
7. A. Prajapati, B. A. Collins, J. D. Goodpaster and M. R. Singh, *Proc. Natl. Acad. Sci.*, 2021, **118**, e2023233118.
8. Y. Song, Y. Zhao, G. Nan, W. Chen, Z. Guo, S. Li, Z. Tang, W. Wei and Y. Sun, *Appl. Catal. B*, 2020, **270**, 118888.
9. N. Spinner and W. E. Mustain, *J. Electrochem. Soc.*, 2013, **160**, F1275.
10. C. Oh, J. Kim, Y. J. Hwang, M. Ma and J. H. Park, *Appl. Catal. B*, 2021, **283**, 119653.
11. R. S. Rocha, R. M. Reis, M. R. Lanza and R. Bertazzoli, *Electrochim. Acta*, 2013, **87**, 606-610.
12. H. Wang, J. Chen, Y. Lin, X. Wang, J. Li, Y. Li, L. Gao, L. Zhang, D. Chao, X. Xiao and J.-M. Lee, *Adv. Mater.*, 2021, **33**, 2008422.
13. E. Ponticorvo, M. Iuliano, C. Cirillo and M. Sarno, *Chem. Eng. J.*, 2023, **451**, 139074.
14. L. Zeng, A. R. Thiruppathi, J. van der Zalm, T. Shi and A. Chen, *J. Mater. Chem. A*, 2022, **10**, 15012-15025.
15. L. Yang, J. Huang, R. Ma, R. You, H. Zeng and Z. Rui, *ACS Energy Lett.*, 2019, **4**, 2945-2951.
16. P. Xiao, Y. Wang, T. Nishitoba, J. N. Kondo and T. Yokoi, *Chem. Commun.*, 2019, **55**, 2896-2899.
17. Y. He, J. Liang, Y. Imai, K. Ueda, H. Li, X. guo, G. Yang, Y. Yoneyama and N. Tsubaki, *Catal. Today*, 2020, **352**, 104-110.
18. M. S. Kim, K. H. Park, S. J. Cho and E. D. Park, *Catal. Today*, 2021, **376**, 113-118.
19. Y. Zhou, H. Wang, X. Liu, S. Qiao, D. Shao, J. Zhou, L. Zhang and W. Wang, *Nano Energy*, 2021, **79**, 105449.
20. L. Yang, J. Huang, J. Cen, D.-L. Chen, H. Zeng, Z. Rui, R. Luque and P. Duan, *J. Mater. Chem. A*, 2021, **9**, 7094-7101.
21. L. Luo, J. Luo, H. Li, F. Ren, Y. Zhang, A. Liu, W.-X. Li and J. Zeng, *Nat. Commun.*, 2021, **12**, 1-10.
22. J. Yang, J. Hao, J. Wei, J. Dai and Y. Li, *Fuel*, 2020, **266**, 117104.
23. Y. Zeng, H. C. Liu, J. S. Wang, X. Y. Wu and S. L. Wang, *Catal. Sci. Technol.*, 2020,

10, 2329-2332.

24. Y. Zhou, L. Zhang and W. Wang, *Nat. Commun.*, 2019, **10**, 1-8.

25. J. Wang, R. Li, D. Zeng, W. Wang, Y. Zhang, L. Zhang and W. Wang, *Chem. Eng. J.*, 2023, **452**, 139505.